



# $\kappa$ TNG: effect of baryonic processes on weak lensing with IllustrisTNG simulations

Ken Osato, Jia Liu, Zoltán Haiman

## ► To cite this version:

Ken Osato, Jia Liu, Zoltán Haiman.  $\kappa$ TNG: effect of baryonic processes on weak lensing with IllustrisTNG simulations. Monthly Notices of the Royal Astronomical Society, 2021, 502 (4), pp.5593-5602. 10.1093/mnras/stab395 . hal-02999504

**HAL Id: hal-02999504**

**<https://hal.science/hal-02999504>**

Submitted on 16 Aug 2022

**HAL** is a multi-disciplinary open access archive for the deposit and dissemination of scientific research documents, whether they are published or not. The documents may come from teaching and research institutions in France or abroad, or from public or private research centers.

L'archive ouverte pluridisciplinaire **HAL**, est destinée au dépôt et à la diffusion de documents scientifiques de niveau recherche, publiés ou non, émanant des établissements d'enseignement et de recherche français ou étrangers, des laboratoires publics ou privés.

# $\kappa$ TNG: effect of baryonic processes on weak lensing with IllustrisTNG simulations

Ken Osato<sup>1</sup>,<sup>★</sup> Jia Liu<sup>2,3</sup> and Zoltán Haiman<sup>4</sup>

<sup>1</sup>*Institut d'Astrophysique de Paris, Sorbonne Université, CNRS, UMR 7095, F-75014 Paris, France*

<sup>2</sup>*Berkeley Center for Cosmological Physics, University of California, Berkeley, CA 94720, USA*

<sup>3</sup>*Lawrence Berkeley National Laboratory, 1 Cyclotron Road, Berkeley, CA 93720, USA*

<sup>4</sup>*Department of Astronomy, Columbia University, New York, NY 10027, USA*

Accepted 2021 February 5. Received 2021 February 2; in original form 2020 October 21

## ABSTRACT

We study the effect of baryonic processes on weak lensing (WL) observables with a suite of mock WL maps, the  $\kappa$ TNG, based on the cosmological hydrodynamic simulations IllustrisTNG. We quantify the baryonic effects on the WL angular power spectrum, one-point probability distribution function (PDF), and number counts of peaks and minima. We also show the redshift evolution of the effects, which is a key to distinguish the effect of baryons from fundamental physics such as dark energy, dark matter, and massive neutrinos. We find that baryonic processes reduce the small-scale power, suppress the tails of the PDF, peak and minimum counts, and change the total number of peaks and minima. We compare our results to existing semi-analytical models and hydrodynamic simulations, and discuss the source of discrepancies. The  $\kappa$ TNG suite includes 10 000 realizations of  $5 \times 5 \text{ deg}^2$  maps for 40 source redshifts up to  $z_s = 2.6$ , well covering the range of interest for existing and upcoming WL surveys. We also produce the  $\kappa$ TNG-Dark suite of maps, generated based on the corresponding dark matter-only IllustrisTNG simulations. Our mock maps are not only suitable for developing analytical models that incorporate the effect of baryons, but also particularly useful for studies that rely on mass maps, such as non-Gaussian statistics and machine learning with convolutional neural networks. The suite of mock maps is publicly available at Columbia Lensing (<http://columbialensing.org>).

**Key words:** gravitational lensing; weak – methods: numerical – large-scale structure of Universe.

## 1 INTRODUCTION

Weak gravitational lensing (WL; for reviews, see Bartelmann & Schneider 2001; Hoekstra & Jain 2008; Kilbinger 2015; Mandelbaum 2018) is a promising cosmological probe of fundamental physics such as the nature of dark energy and dark matter, theory of gravity, and the mass sum of neutrinos. By measuring the distortion in shapes of background galaxies caused by the foreground matter, we can infer the intervening large-scale structure. Ongoing Stage-III WL surveys, such as the Subaru Hyper Suprime-Cam (Aihara et al. 2018; Mandelbaum et al. 2018; Hikage et al. 2019), Dark Energy Survey (DES; Dark Energy Survey Collaboration 2016; Abbott et al. 2018), and Kilo Degree Survey (KiDS; de Jong et al. 2015; Hildebrandt et al. 2017; Heymans et al. 2021), have already achieved competitive cosmological constraints. Stage-IV cosmological surveys, such as the Vera C. Rubin Observatory Legacy Survey of Space and Time (LSST; LSST Science Collaboration 2009), and large-area surveys by *Euclid* (Amendola et al. 2018), and the *Nancy Grace Roman Space Telescope*,<sup>1</sup> are expected to revolutionize our understanding of the cosmos as well as fundamental physics, enabled by their large sky coverage and deep photometry.

In order to realize the full potential of ongoing and upcoming WL surveys, we urgently need to improve our understanding of

baryonic physics (see a recent review by Chisari et al. 2019). Baryonic processes during galaxy formation, such as radiative cooling, feedback from black hole accretion, star formation, and supernova feedback, redistribute the gas inside a halo and reshape its gravitational potential. Signals from these astrophysical processes can mimic those expected from varying cosmological parameters, causing biases in our parameter inference if left untreated (Rudd, Zentner & Kravtsov 2008; Semboloni et al. 2011; Zentner et al. 2013; Mohammed et al. 2014; Harnois-Déraps et al. 2015; Osato, Shirasaki & Yoshida 2015; Huang et al. 2019). At low redshift relevant to most WL surveys, the effects of baryons are predominately due to black hole activities, manifested as a  $\gtrsim 10$  per cent level suppression in clustering around Mpc scale, though the exact level and its redshift and scale dependence remain ill-constrained. As a result, current WL surveys often need to apply aggressive scale cuts to mitigate contamination from baryonic effects. For example, DES applied lower limits as large as a few  $\times 10$  arcmin in some redshift bins in analysing their Y1 data, discarding well-measured smaller scale data (Abbott et al. 2018). This strategy will not be sustainable for Stage-IV surveys, which will provide high-precision measurements on subarcmin scales. Recently, Huang et al. (2021) have extended their analysis to smaller scales with the same DES Y1 data, by modelling and marginalizing over baryonic feedback using a principal component analysis (PCA) method based on 11 hydrodynamic simulations. With a 2.5 arcmin scale cut, they already found a 20 per cent improvement on the  $S_8 = \sigma_8(\Omega_m/0.3)^{0.5}$  constraint.

\* E-mail: [ken.osato@iap.fr](mailto:ken.osato@iap.fr)

<sup>1</sup> <https://roman.gsfc.nasa.gov>

Existing works in modelling the baryonic effects mainly focus on their impact on the two-point statistics – the correlation function, or its Fourier transform, the power spectrum – of the 3D matter distribution and of the 2D WL shear or convergence. These approaches incorporate the baryonic effects as free parameters that either alter the halo mass–concentration relation based on the halo model (Cooray & Sheth 2002; Yang et al. 2013; Mead et al. 2015), modify the gas, stellar, and dark matter density components separately (Schneider et al. 2019, 2020; Aricò et al. 2020b), quantify the changes on the full power spectrum as PCAs (Eifler et al. 2015; Huang et al. 2019), or displace the matter following a pressure-like potential (Dai, Feng & Seljak 2018). All these methods are calibrated against observations and/or hydrodynamic simulations.

Recently, it has been recognized that non-Gaussian WL statistics contain rich information beyond the traditional two-point statistics and that they will be a powerful tool in constraining cosmological parameters. This has been partly demonstrated in Stage-II and Stage-III surveys (Liu et al. 2015a, b; Kacprzak et al. 2016; Martinet et al. 2018; Shan et al. 2018). However, the study of baryonic effects on non-Gaussian statistics has been limited mainly due to the lack of analytical theories. Therefore, these studies typically rely on simulated WL maps to investigate baryonic effects on various non-Gaussian statistics: three-point correlation (Semboloni, Hoekstra & Schaye 2013; Aricò et al. 2020a; Foreman et al. 2020), peak statistics (Yang et al. 2013; Osato et al. 2015), and minima counts (Coulton et al. 2020).

Hydrodynamic simulations are currently the state-of-the-art tool to study baryonic physics. In these simulations, baryonic processes are modelled with subgrid prescriptions, enabling us to capture the non-linear astrophysics over a wide dynamic range (for reviews, see Somerville & Davé 2015; Vogelsberger et al. 2020). Mock WL maps generated from hydrodynamic simulations are a critical component in studying the effect of baryons on WL observables.

In this paper, we introduce  $\kappa$ TNG, a suite of mock WL maps generated from the IllustrisTNG simulations. We quantify the baryonic effects on WL statistics including the angular power spectrum, peak counts, counts of minima, and the probability distribution function (PDF). We compare them to those measured from the corresponding dark matter-only (DMO) simulations,  $\kappa$ TNG-Dark, which adopts the same initial condition but without baryonic physics. In addition, we compare our results to existing analytical models as well as other hydrodynamic simulations.

This paper is organized as follows. In Section 2, we describe our numerical methods to generate mock WL maps from the existing IllustrisTNG simulations. We present in Section 3 our results of the baryonic effects on WL statistics by comparing the  $\kappa$ TNG and  $\kappa$ TNG-Dark pairs. We show their redshift dependence as well as comparisons to existing models and other hydrodynamic simulations. We summarize our main conclusions in Section 4.

## 2 NUMERICAL SIMULATIONS

In this section, we briefly describe the underlying IllustrisTNG hydrodynamic simulations and the ray-tracing methodology we follow to generate the  $\kappa$ TNG mock WL maps. Throughout this paper, we adopt a flat  $\Lambda$  cold dark matter Universe at the *Planck* 2015 cosmology (Planck Collaboration XIII 2016), as used in the IllustrisTNG simulations, with Hubble constant  $H_0 = 67.74 \text{ km s}^{-1} \text{ Mpc}^{-1}$ , baryon density  $\Omega_b = 0.0486$ , matter density  $\Omega_m = 0.3089$ , spectral index of scalar perturbations  $n_s = 0.9667$ , and amplitude of matter fluctuations at  $8 h^{-1} \text{ Mpc}$   $\sigma_8 = 0.8159$ . We assume massless neutrinos, with an effective number of neutrino species  $N_{\text{eff}} = 3.046$ .

### 2.1 IllustrisTNG hydrodynamic simulations

Because galaxy formation involves a wide dynamic range – from structures internal to stars to beyond the virial radii of the largest haloes – it is impossible to resolve all the relevant physical processes simultaneously in a cosmological simulation. Therefore, baryonic processes are typically approximated by subgrid prescriptions, in which empirical recipes are implemented to inject or remove energy and momentum from regions of the simulation box when certain conditions are met. Recent cosmological hydrodynamic simulations, such as the Horizon-AGN (Dubois et al. 2014), EAGLE (Schaye et al. 2015), BAHAMAS (McCarthy et al. 2017, 2018), Illustris (Vogelsberger et al. 2014), and its successor IllustrisTNG simulations (Marinacci et al. 2018; Naiman et al. 2018; Nelson et al. 2018, 2019; Pillepich et al. 2018; Springel et al. 2018), have already provided invaluable insights into the impact of baryons on cosmological observables.

In this work, we use the IllustrisTNG simulations as our base. They are a set of cosmological, large-scale gravity and magneto-hydrodynamical simulations generated with the moving mesh code AREPO (Springel 2010). Subgrid prescriptions are incorporated into model stellar evolution, chemical enrichment, gas cooling, and black hole feedback (Pillepich et al. 2018). The full simulation set includes three box sizes, each with simulations of different resolutions. Here, we employ the highest resolution simulation for the largest box, TNG300-1 (hereafter TNG), which covers a comoving volume of  $(205 h^{-1} \text{ Mpc})^3$ . It has a mass resolution of  $7.44 \times 10^6$  and  $3.98 \times 10^7 h^{-1} M_\odot$  for initial gas and dark matter particles, respectively. To discriminate baryonic effects, we make use of the corresponding DMO simulations TNG300-1-Dark (hereafter TNG-Dark), which has a mass resolution of  $4.73 \times 10^7 h^{-1} M_\odot$  for DM particles. TNG and TNG-Dark have the same initial conditions and only differ in the inclusion of baryonic physics. These simulations accurately resolve the small-scale, non-linear gravitational evolution of the matter density field that is accessible by Stage-IV cosmological surveys.

To study the WL observables, we need to generate mock maps with a reasonable area (at least a few  $\text{deg}^2$ ) and redshift coverage (up to  $z \approx 2$ ). In addition, a large number of realizations are important to suppress cosmic variance. The TNG simulation snapshots are outputted at 99 redshifts between  $z = 0$  and 20, allowing one to build light-cones that are necessary to construct mock WL maps. However, since IllustrisTNG was not tailored to build mock WL maps, we must overcome some difficulties to achieve our goal. First, these snapshots are not output at regular intervals of comoving distance, as would have been required for standard WL ray-tracing schemes (Dietrich & Hartlap 2010; Harnois-Déraps et al. 2018; Liu et al. 2018; Harnois-Déraps, Giblin & Joachimi 2019). Secondly, the box size, despite being very large for hydrodynamic simulations, is relatively small compared to the usual DMO cosmological simulations; hence, it can only cover a small patch of the sky at high redshifts. Finally, due to the high computational cost, only one simulation was generated at the box size and resolution we need. We adapt our ray-tracing method to accommodate these pre-existing settings, which we describe in detail next.

### 2.2 $\kappa$ TNG: ray-traced WL mock maps

To build a light-cone, we stack the TNG snapshots along the line of sight in a fixed interval of  $205 h^{-1} \text{ Mpc}$  (= TNG box size). The comoving distance between  $z = 0$  and  $z \approx 2.5$  is approximately  $4000 h^{-1} \text{ Mpc}$ , which requires 20 boxes in total to cover. We select

**Table 1.** Summary of our light-cone. Columns: (1) snapshot number; (2) comoving distance and (3) redshift at the snapshot centre; (4) corresponding TNG snapshot redshift and (5) TNG file number.

Snapshot	$\chi$ ( $h^{-1}$ Mpc)	$z$	$z^{\text{TNG}}$	TNG file
1	102.5	0.034	0.03	96
2	307.5	0.105	0.11	90
3	512.5	0.179	0.18	85
4	717.5	0.255	0.26	80
5	922.5	0.335	0.33	76
6	1127.5	0.418	0.42	71
7	1332.5	0.506	0.50	67
8	1537.5	0.599	0.60	63
9	1742.5	0.698	0.70	59
10	1947.5	0.803	0.79	56
11	2152.5	0.914	0.92	52
12	2357.5	1.034	1.04	49
13	2562.5	1.163	1.15	46
14	2767.5	1.302	1.30	43
15	2972.5	1.452	1.41	41
16	3177.5	1.615	1.60	38
17	3382.5	1.794	1.82	35
18	3587.5	1.989	2.00	33
19	3792.5	2.203	2.21	31
20	3997.5	2.440	2.44	29

the TNG snapshots that are the closest to the centres of the 20 light-cone intervals, if they were equally spaced in comoving distance.<sup>2</sup> We summarize our light-cone configuration in Table 1, including the comoving distance  $\chi$  and redshift for each snapshot, as well as the corresponding TNG file. We illustrate our light-cone configuration in Fig. 1. The opening angle of the light-cone is  $5 \times 5 \text{ deg}^2$ . The last 10 snapshots are replicated 4 times in the transverse direction, so that we can cover the desired map size ( $5 \times 5 \text{ deg}^2$ ) at the highest redshift maps. Our light-cone extends up to redshift  $z = 2.57$ . We construct mock WL maps at 40 source redshifts using this light-cone.

To model the propagation of light rays in our light-cone, we employ a multiple-lens plane approximation (Blandford & Narayan 1986; Seitz, Schneider & Ehlers 1994; Jain, Seljak & White 2000; Vale & White 2003; Hilbert et al. 2009), where the smooth matter distribution is approximated as discrete density planes of thickness  $\Delta\chi$ . Light rays originating from the observer at  $z = 0$  are deflected only at the planes and travel in straight lines between the planes. At the angular position  $\beta^k$  at the  $k$ -th plane, the deflection angle  $\alpha$  is the gradient of the 2D lensing potential  $\psi$ :

$$\alpha^k(\beta^k) = \nabla_{\beta^k} \psi^k(\beta^k). \quad (1)$$

The lensing potential can be computed from the Poisson equation:

$$\nabla_{\beta^k}^2 \psi^k(\beta^k) = 2\sigma^k(\beta^k), \quad (2)$$

where the dimensionless surface density  $\sigma^k$  is the projected matter distribution of the  $k$ -th lens plane:

$$\sigma^k(\beta^k) = \frac{3H_0^2\Omega_m}{2c^2} \frac{\chi^k}{a^k} \int_{\chi^k - \Delta\chi/2}^{\chi^k + \Delta\chi/2} \delta(\beta^k, \chi') d\chi, \quad (3)$$

<sup>2</sup>In principle, we could use all 100 TNG snapshots in generating our light-cone. However, we expect negligible differences between 2 and 3 consecutive snapshots and hence we limited the number of snapshots to 20 in total for faster data transfer and computation.

where  $c$  is the speed of light,  $a$  is the scale factor, and  $\delta = (\rho - \bar{\rho})/\bar{\rho}$  is the three-dimensional matter overdensity. The lensed position  $\beta^k$  is the sum of previous deflection angles:

$$\beta^k(\theta) = \theta - \sum_{i=1}^{k-1} \frac{\chi^k - \chi^i}{\chi^k} \alpha^i(\beta^i), \quad (k = 2, 3, \dots) \quad (4)$$

where we impose  $\beta^0 = \beta^1 = \theta$  for initial rays. By differentiating  $\beta^k$  with respect to  $\theta$ , we can obtain the distortion matrix that maps the initial position to the lensed position  $\theta \rightarrow \beta$ :

$$A_{ij}(\theta, \chi) \equiv \frac{\partial \beta_i(\theta, \chi)}{\partial \theta_j} = \begin{pmatrix} 1 - \kappa - \gamma_1 & -\gamma_2 + \omega \\ -\gamma_2 - \omega & 1 - \kappa + \gamma_1 \end{pmatrix}, \quad (5)$$

where, for legibility, we suppressed the dependence on  $(\theta, \chi)$  for the convergence  $\kappa$ , the shear components  $\gamma_1$  and  $\gamma_2$ , and the rotation  $\omega$ . To obtain  $\beta$  and  $A_{ij}$ , we employ a memory-efficient ray-tracing scheme developed in Hilbert et al. (2009), where the computation for the  $k$ -th plane depends only on the quantities at  $(k-1)$ th and  $(k-2)$ th planes.

The configurations of our source planes and lens planes are illustrated in Fig. 1. We also summarize the corresponding comoving distances and redshifts in Table 2. We divide each snapshot into two density slices of thickness  $\Delta\chi = 102.5 h^{-1} \text{ Mpc}$ . We then project each slice on to a regular grid of  $4096^2$  pixels. The dark matter, gas, and star particles (in the case of TNG-Dark, only dark matter particles) are assigned to the grid with a triangular-shaped cloud scheme. Next, we apply a fast Fourier transform (FFT) to equation (2) to obtain the derivatives of the lensing potential. We evaluate the deflection angle and the distortion matrix at the angular position  $\beta^k$  and generate  $(\kappa, \gamma_1, \gamma_2, \omega)$  maps at each source plane. Each map is on a regular grid with  $1024^2$  pixels, corresponding to a pixel size of 0.29 arcmin. In total, we generate 40 source planes. Note that  $i$ -th lens plane contains the contribution from the range  $(\chi^i - \Delta\chi/2, \chi^i + \Delta\chi/2)$ , but observables (e.g.  $\beta^i$ ) are defined at  $\chi^i$ . Thus, the  $i$ -th source plane, where the observables are output, is placed at  $\chi^i + \Delta\chi/2$ .

To suppress sample variance, we need a large number of map realizations. To accomplish this goal with only one simulation of TNG, we exploit the periodic boundary condition and the fact that the light-cone does not cover the whole simulation box. We construct *pseudo-independent* map realizations by randomly translating and rotating the snapshots. First, for each snapshot, we (1) translate all particles by a random number along each of the three axes, (2) rotate the snapshot by 0, 90, 180, or 270 deg around each of the three axes, and (3) apply a random flip along any of the three axes. We repeat this process 100 times and generate lensing potential planes from these randomized snapshots. Next, for each lens plane set, we further translate and rotate the planes randomly, for 100 times. Finally, we obtain 10 000 pseudo-independent realizations. Such procedure has been studied thoroughly in the past by Petri, Haiman & May (2016), who found that even with only one simulation, the snapshots can be repeatedly recycled to produce up to a few  $\times 10^4$  WL map realizations whose power spectra and high-significance peak counts can be treated as statistically independent. Such a large number of realizations would also allow the application of machine learning to study the mapping from the DMO to hydrodynamic WL maps.

### 3 RESULTS

In Fig. 2, we show an example of  $\kappa$ TNG map at  $z_s = 1.034$  (S23), as well as the difference between the pair of hydrodynamic



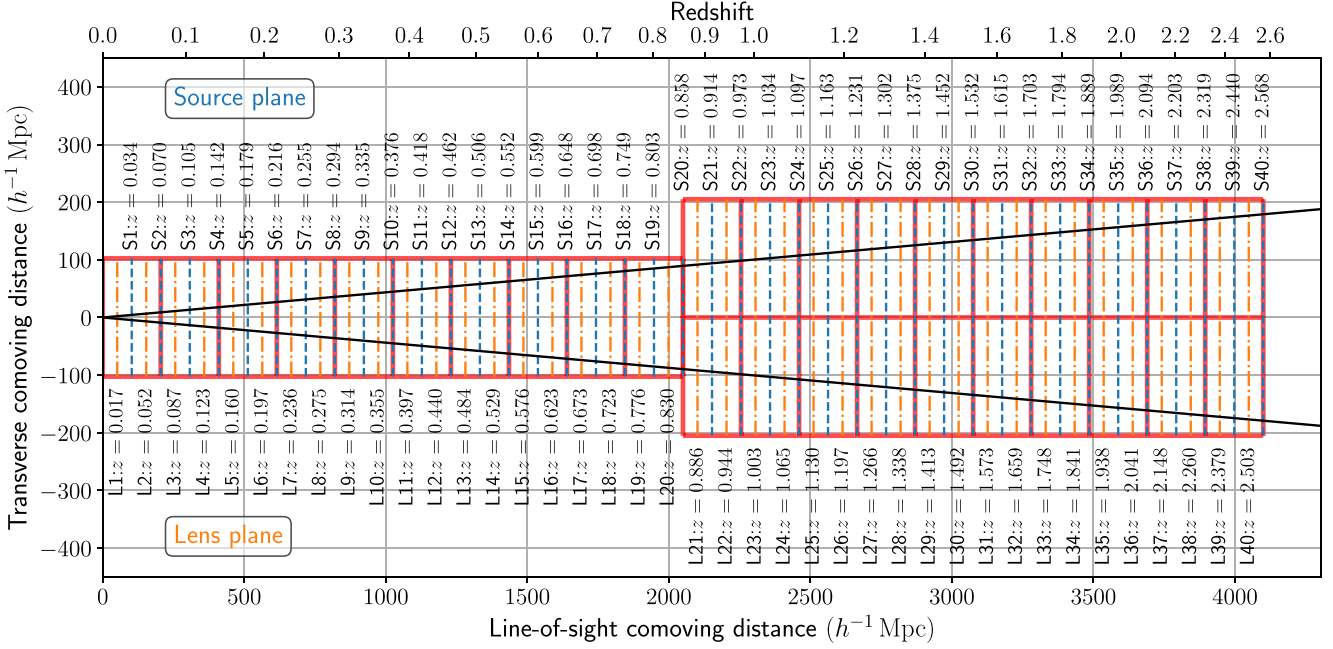


**Figure 1.** The construction of our light-cone. Each red box corresponds to one snapshot. The last 10 snapshots are replicated 4 times (twice in each transverse direction) to increase the solid area to cover  $5 \times 5$  deg. Each box is divided into two lens planes of  $\Delta\chi = 102.5 h^{-1}$  Mpc thickness. We list the redshifts at the central positions of source (blue dashed lines) and lens (orange dash-dotted lines) planes. The black lines correspond to our opening angle of 5 deg. We generate lensing mocks at 40 source redshifts.

and DMO maps. The amplitude of the difference appears to be correlated with the  $\kappa$  values of the pixels, but in a somewhat complex fashion. For example, some dipole patterns are clearly seen in the overdense regions. In most baryonification models, e.g. HMcode (Mead et al. 2015) and baryonic correction models (e.g. Schneider & Teyssier 2015; Schneider et al. 2019), the halo positions, or clustering properties, are assumed to be unchanged due to baryonic effects. It may be caused by collimated active galactic nucleus (AGN) jets or changes in halo positions and ellipticities. We leave a thorough investigation to future work. Next, we quantify these effects with the power spectrum, PDF, and peak and minimum counts. Together, they capture both Gaussian and non-Gaussian information and are complementary probes for cosmology.

### 3.1 Power spectrum

We measure the angular power spectra of the convergence map  $C_\kappa$  using a binned estimator:

$$C_\kappa(\ell_i) = \frac{1}{N_i} \sum_{|\ell| \in [\ell_i^{\min}, \ell_i^{\max}]} |\tilde{\kappa}(\ell)|^2, \quad (6)$$

where  $\ell_i$  is the mean of multipoles in the  $i$ -th bin with bounds  $[\ell_i^{\min}, \ell_i^{\max}]$ ,  $N_i$  is the number of modes, and  $\tilde{\kappa}(\ell)$  is the Fourier transform of the convergence field, computed on a  $1024^2$  regular grid with FFT. We assign 10 log-equally spaced bins in the range of  $[10^2, 10^3]$  and 20 log-equally spaced bins in the range of  $[10^3, 10^4]$  – in total 30 multipole bins.

We first validate our ray-tracing code by comparing the  $\kappa$ TNG-Dark power spectra with the theoretical prediction from *halofit* (Smith et al. 2003; Takahashi et al. 2012). We show the comparison for all 40 source redshifts in Fig. 3. On large scales ( $\ell \approx$  a few  $\times 100$ ), our measured power spectra are lower than the theoretical prediction by  $\approx 5$  per cent. The reduced power reflects the missing

large-scale modes due to the limited TNG box size. However, since both the  $\kappa$ TNG and  $\kappa$ TNG-Dark maps are impacted by this effect on the same footing, it is expected to be cancelled out when we consider the differences between the simulation pair. Note that, for lower source redshifts, the statistical variance is so large that the measured power spectrum can be accidentally closer to the *halofit* results. On small scales ( $\ell > 1000$ ), the differences for  $z_s > 0.4$  curves are within the known *halofit* modelling uncertainty of  $\approx 10$  per cent. For low redshifts  $z_s < 0.4$ , the discrepancies become larger, because the same  $\ell$  value corresponds to smaller structures, some of which are below the simulation resolution. To investigate the effect of map resolution, we generate 50 additional high-resolution test maps with number of grids doubled at a side. The fiducial power spectra are consistent with these high-resolution maps within 1 per cent for  $100 < \ell < 5000$ , but are suppressed by  $\approx 5$  per cent at  $\ell = 10000$  for  $z_s = 1.034$  (S23), and the suppression at  $\ell = 10000$  becomes larger for lower source redshift. However,  $\kappa$ TNG and  $\kappa$ TNG-Dark maps are affected by the resolution in the same manner, and thus, the angular power spectrum ratio is not subject to the resolution effect.<sup>3</sup> Finally, we note that the *halofit* model was calibrated against simulations with lower resolution than the TNG and is known to overpredict the WL power on small scales, so it should only be considered as a rough estimate in this regime (see e.g. Mead et al. 2015; Wei et al. 2018).

We investigate the effect of baryons on the WL power spectrum next. In Fig. 4, we present the redshift evolution of the  $\kappa$ TNG power spectrum in the upper panel, as well as the fractional differences between the  $\kappa$ TNG and  $\kappa$ TNG-Dark maps in the lower panel. Both the power spectra and ratios are averaged over  $N_r = 10000$

<sup>3</sup>The suppression in the power spectrum due to resolution can be corrected by introducing a damping factor (Takahashi et al. 2017). However, we do not apply this damping factor because it does not take into account the redshift dependence and we are interested mainly in the angular power spectrum ratio.

**Table 2.** The comoving distance  $\chi$  and redshifts ( $z_s, z_l$ ) for our source and lens planes. The light-cone configuration is illustrated in Fig. 1.

Source plane	$\chi$ ( $h^{-1}$ Mpc)	$z_s$	Lens plane	$\chi$ ( $h^{-1}$ Mpc)	$z_l$
S1	102.5	0.034	L1	51.25	0.017
S2	205.0	0.070	L2	153.75	0.052
S3	307.5	0.105	L3	256.25	0.087
S4	410.0	0.142	L4	358.75	0.123
S5	512.5	0.179	L5	461.25	0.160
S6	615.0	0.216	L6	563.75	0.197
S7	717.5	0.255	L7	666.25	0.236
S8	820.0	0.294	L8	768.75	0.275
S9	922.5	0.335	L9	871.25	0.314
S10	1025.0	0.376	L10	973.75	0.355
S11	1127.5	0.418	L11	1076.25	0.397
S12	1230.0	0.462	L12	1178.75	0.440
S13	1332.5	0.506	L13	1281.25	0.484
S14	1435.0	0.552	L14	1383.75	0.529
S15	1537.5	0.599	L15	1486.25	0.576
S16	1640.0	0.648	L16	1588.75	0.623
S17	1742.5	0.698	L17	1691.25	0.673
S18	1845.0	0.749	L18	1793.75	0.723
S19	1947.5	0.803	L19	1896.25	0.776
S20	2050.0	0.858	L20	1998.75	0.830
S21	2152.5	0.914	L21	2101.25	0.886
S22	2255.0	0.973	L22	2203.75	0.944
S23	2357.5	1.034	L23	2306.25	1.003
S24	2460.0	1.097	L24	2408.75	1.065
S25	2562.5	1.163	L25	2511.25	1.130
S26	2665.0	1.231	L26	2613.75	1.197
S27	2767.5	1.302	L27	2716.25	1.266
S28	2870.0	1.375	L28	2818.75	1.338
S29	2972.5	1.452	L29	2921.25	1.413
S30	3075.0	1.532	L30	3023.75	1.492
S31	3177.5	1.615	L31	3126.25	1.573
S32	3280.0	1.703	L32	3228.75	1.659
S33	3382.5	1.794	L33	3331.25	1.748
S34	3485.0	1.889	L34	3433.75	1.841
S35	3587.5	1.989	L35	3536.25	1.938
S36	3690.0	2.094	L36	3638.75	2.041
S37	3792.5	2.203	L37	3741.25	2.148
S38	3895.0	2.319	L38	3843.75	2.260
S39	3997.5	2.440	L39	3946.25	2.379
S40	4100.0	2.568	L40	4048.75	2.503

realizations.<sup>4</sup> In general, a spoon-like feature is seen. At large scales, the ratio is close to unity, i.e. no significant baryonic effects. On small scales, a suppression up to 20 per cent is seen. This is mainly because feedback processes such as feedback from black hole accretion and supernova explosions, which can remove gas from the halo centre, reduce the matter clustering on relevant scales. The location of the dip moves from small angular scales at high redshift to larger angular scales ( $\ell \approx 1000$ ) at lower redshift, mainly because the same physical scales extend larger angles at lower redshift. In addition, at low redshift, baryonic feedback is also more powerful, reaching further in physical scales. Finally, the upturn seen at much smaller scales is the result of radiative cooling, which enhances the matter clustering. In Appendix A, we present a fitting formula for the suppression due to baryons on the angular power spectrum.

<sup>4</sup>We take the mean of ratio, instead of the ratio of the mean power spectra, to reduce the cosmic variance.

The characteristic shape of the baryonic effects on the WL power spectrum mimics the effect of changing cosmological parameters, in particular the mass sum of neutrinos, which also shows a spoon-like feature (Lesgourgues & Pastor 2006; Hannestad, Upadhye & Wong 2020). The key to distinguish them is their different redshift and scale dependence. In addition, they may also manifest differently in other statistics beyond the power spectrum, such as the ones we study next.

### 3.2 PDF

Here, we present the effect of baryons on the WL one-point PDF. Past studies of the WL PDF have shown that it has the potential to significantly tighten the cosmological constraints, compared to using the power spectrum alone (Wang, Haiman & May 2009; Liu et al. 2016; Patton et al. 2017; Liu & Madhavacheril 2019). Recently, Thiele, Hill & Smith (2020) developed an analytical model for the WL one-point PDF and its autocovariance, based on a halo-model formalism. While baryonic effects have not been included in these studies, future extensions could incorporate baryonic effects.

We first smooth the maps with a  $\theta_G = 2$  arcmin Gaussian window to suppress small-scale noise. The window function is given as

$$W(\theta) = \frac{1}{\pi\theta_G^2} \exp\left(-\frac{\theta^2}{\theta_G^2}\right). \quad (7)$$

We exclude pixels within  $2\theta_G$  from the edge due to incomplete smoothing. To measure the PDF, we then measure the histogram of the pixels, binned by their  $\kappa$  value with the bin width  $\Delta\kappa = 0.025$ .<sup>5</sup> In Fig. 5, we present the redshift evolution of the  $\kappa$ TNG PDF in the upper panel, as well as the fractional differences between the  $\kappa$ TNG and  $\kappa$ TNG-Dark maps in the lower panel. The PDF is skewed with a high- $\kappa$  tail for all redshifts considered in our work, indicating the non-Gaussian information that is not captured by the power spectrum.

The primary effect of baryonic processes is the suppression of the intermediate positive  $\kappa$  and negative  $\kappa$  regions, as well as an enhancement at the very high  $\kappa$  tail. In the intermediate positive convergence regime, feedback processes tend to expel the gas from overdense regions, resulting in a suppression of the most clustered, non-linear structures. Consequently, even the void regions can acquire some mass, resulting in the observed decrease in the number of highly negative pixels. The redistribution of matter by baryonic effects smoothes the overall density fluctuation, resulting in more pixels with small convergence ( $\kappa \approx 0$ ) signals. The enhancement at the very high  $\kappa$  tail is due to radiative cooling.

### 3.3 Peaks and minima

The number count of WL peaks – pixels with a higher value than their surrounding eight pixels – is the most well-studied non-Gaussian statistic (e.g. Dietrich & Hartlap 2010; Kratochvil, Haiman & May 2010). It has been applied to observational data from the CFHTLenS (Liu et al. 2015a), CS82 (Liu et al. 2015b), DES (Kacprzak et al. 2016), and KiDS surveys (Martinet et al. 2018; Shan et al. 2018) and returned comparable or better constraints to those from the two-point statistics. The convergence peaks

<sup>5</sup>To account for the slight (de)magnification of the ray bundles during ray tracing, we weigh the pixels by the inverse magnification in computing the PDF. Since smoothing smears the small-scale structures, the PDFs from high-resolution and fiducial maps are consistent within 1 per cent. We expect this to have negligible effect on our results. The smoothing further reduces its effect. See more discussion in Takahashi et al. (2011).

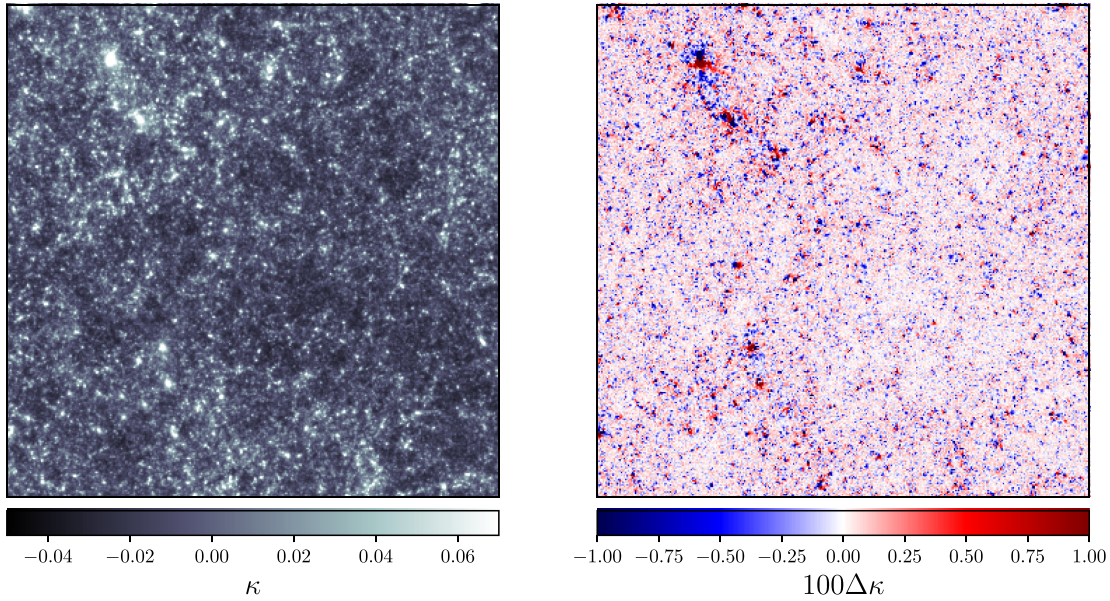


**Figure 2.** Left-hand panel: An example of  $\kappa$ TNG convergence map at source redshift  $z_s = 1.034$ . Right-hand panel: The difference between the paired  $\kappa$ TNG and  $\kappa$ TNG-Dark maps  $\Delta\kappa = \kappa^{\kappa\text{TNG}} - \kappa^{\kappa\text{TNG-Dark}}$ . They have the same initial conditions, but the baryonic processes are only included in the former. The  $\kappa$ TNG-Dark map is not shown here as it is almost indistinguishable from the  $\kappa$ TNG map. All our maps are  $5 \times 5 \text{ deg}^2$  in size, each on a  $1024^2$  regular grid corresponding to a pixel size of 0.29 arcmin.

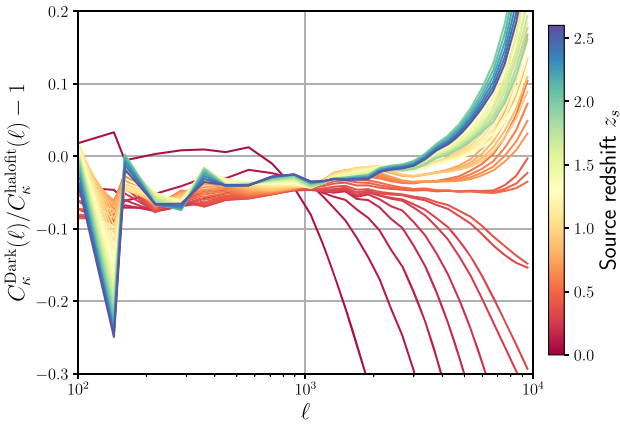


**Figure 3.** The fractional differences of the  $\kappa$ TNG-Dark power spectra with respect to the analytical *halofit* predictions. The result for the first source redshift  $z_s = 0.034$  is not shown due to large statistical uncertainty.

originate from single massive haloes or superpositions of multiple intermediate-mass haloes (Yang et al. 2011; Liu & Haiman 2016). They are sensitive to both the growth of structure and the expansion history of the universe. In contrast, WL minima – pixels with a lower value than their surrounding eight pixels – also contain information complementary to peaks (Maturi et al. 2010; Coulton et al. 2020). WL peaks and minima are easily measurable in WL mass maps, without the need to identify physical structures such as clusters or voids. Past works studying the baryonic effects on WL peaks and minima have found that they are affected differently than the power spectrum (Yang et al. 2013; Osato et al. 2015; Weiss et al. 2019; Coulton et al. 2020), in terms of biases in cosmological parameters. Therefore, they can also serve as a tool to calibrate potential systematics. Compared to the simulations used in previous studies, the  $\kappa$ TNG mock WL

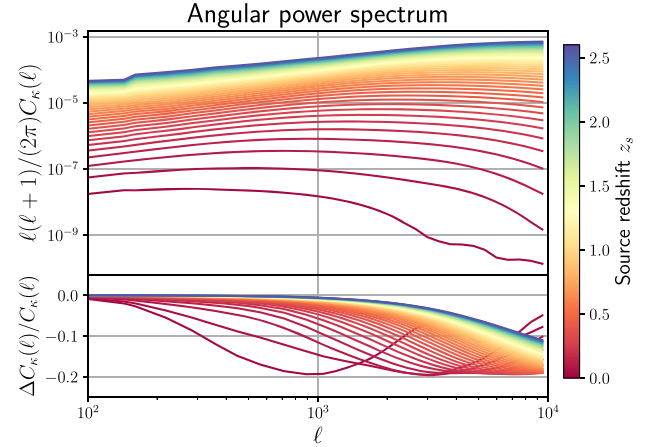


**Figure 4.** Upper panel: Angular power spectra for all source redshifts from our  $\kappa$ TNG maps (red to blue: low to high redshifts). We do not show the curves for  $\kappa$ TNG-Dark maps, as they are almost indistinguishable by eye from the  $\kappa$ TNG curves. Lower panel: Fractional differences between the  $\kappa$ TNG and  $\kappa$ TNG-Dark power spectra for all 40 source redshifts, where  $\Delta C_k/C_k = C_k^{\kappa\text{TNG}}/C_k^{\kappa\text{TNG-Dark}} - 1$ . The power spectra and ratios are means over 10 000 map realizations. The spectra between  $\ell = 3771.0$ – $9465.6$  for the first source redshift  $z_s = 0.034$  are not shown because of strong artefacts due to resolution.

maps cover a wide range of redshifts and take advantage of the state-of-the-art subgrid models developed by the TNG team.

In Fig. 6, we show the number counts of peaks and minima in the upper panels, as well as the fractional differences between the  $\kappa$ TNG and  $\kappa$ TNG-Dark maps in the lower panels. To measure the number counts of peaks and minima, we again smooth the convergence maps with a  $\theta_G = 2$  arcmin Gaussian window. The peaks and minima are counted in equally spaced bins with a width ( $\Delta\kappa$ ) of 0.025. Similarly



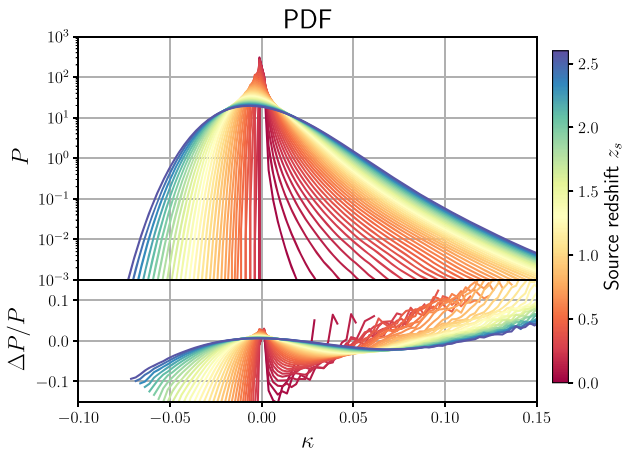


**Figure 5.** Upper panel: The PDFs for all source redshifts from our  $\kappa$ TNG maps (red to blue: low to high redshifts). Lower panel: Fractional differences between the  $\kappa$ TNG and  $\kappa$ TNG-Dark maps for all 40 source redshifts, where  $\Delta P/P = P^{\kappa\text{TNG}}/P^{\kappa\text{TNG-Dark}} - 1$ . The maps are smoothed with a 2 arcmin Gaussian filter. The PDFs and ratios are means over 10 000 map realizations.

to PDFs, pixels within  $2\theta_G$  from the edge are discarded, and the results with high-resolution and fiducial maps are consistent within 1 per cent. The overall baryonic effects in peaks and minimum counts are somewhat similar to that in PDF: Both the positive and negative tails are suppressed. However, we also see an additional effect of reduced number of peaks or minima in contrast to the PDF, which is always normalized to unity. These findings are consistent with previous studies (Osato et al. 2015; Coulton et al. 2020), though the amplitude of the change depends on the strength of the baryonic feedback implemented in the underlying hydrodynamic simulations. We compare our results to previous works, including both (semi-)analytical models and other hydrodynamic simulations, in the next subsection.

### 3.4 Comparison with previous studies

We compare our results to previous works, including analytical models for the power spectrum from the HMcode (Mead et al. 2015) and cosmological hydrodynamic simulations, BAHAMAS (McCarthy et al. 2017, 2018) and Horizon-AGN (Dubois et al. 2014; Gouin et al. 2019). We show the comparison for the power spectrum, PDF, peaks, and minima in Fig. 7. All maps are smoothed with a 2 arcmin Gaussian window for the PDF, peaks, and minima. All our comparisons are done for  $z_s = 1$ , which is close to the expected mean redshift of source galaxies expected from Stage-IV surveys (LSST Science Collaboration 2009; Laureijs et al. 2011).

We compare our results to the *halofit*-based HMcode model using several sets of parameters, all calibrated against different runs of the OWLS simulations (Schaye et al. 2010; van Daalen et al. 2011), including (1) DMONLY, in which only gravity from dark matter is implemented and no baryonic physics is included, (2) REF, in which radiative cooling and heating, star formation and evolution, chemical enrichment, and supernova feedback are included, (3) DBLIM, which adopts a top-heavy initial mass function and stronger supernova feedback in addition to the REF model, and (4) AGN, which includes feedback due to AGNs to the REF model. In addition, we compare our results to two other hydrodynamic simulations. For BAHAMAS, there are 10 000 maps at source redshift  $z_s = 1$ , where each covers  $5 \times 5 \text{ deg}^2$  sky and has a resolution of 0.17 arcmin per pixel. In

addition to the fiducial model, there are two additional runs, where AGN feedback is tuned to be more ('high AGN') or less ('low AGN') effective. These simulations are useful to address the impact of AGN feedback. For Horizon-AGN, there is only one map at  $z_s = 1$  and only power spectrum information is available. Because the simulations adopt different cosmological parameters, it is infeasible to directly compare the statistics. Therefore, we focus only on the ratio of statistics between the hydrodynamic and corresponding DMO simulations.

For the power spectrum, the suppression at scales  $1000 \lesssim \ell \lesssim 5000$  seen in  $\kappa$ TNG is comparable to that from Horizon-AGN, BAHAMAS 'low AGN', and HMcode REF. However, at smaller scales, the amplitude of the suppression is larger for  $\kappa$ TNG, which is caused by the strong AGN feedback implemented in IllustrisTNG. This feature is in general agreement with past results of matter power spectrum (Chisari et al. 2019) and baryon fractions in massive haloes (van Daalen, McCarthy & Schaye 2020). For the PDF, the overall trends are similar between TNG and BAHAMAS. The slightly different zero-crossing is likely due to their different cosmologies and feedback models and hence the overall skewness and width of the PDFs. For peaks and minima, it is interesting to see that the overall baryonic effects are quite similar between the TNG and BAHAMAS, despite the very different subgrid models implemented in them. In particular, the TNG results are comparable to the 'low AGN' run. In addition, Yang et al. (2013) studied the baryonic effects on peak counts by manually boosting the halo concentration by 50 per cent. They found that low peaks are less affected, as these peaks are typically associated with several small haloes along the line-of-sight direction and sensitive to only the outer regions of these haloes, while high peaks are sensitive to the inner regions of single massive haloes. In contrast, we find that low peaks are equally impacted by baryons, an evidence that baryons are impacting small haloes beyond their virial radii.

Within the current observational limit, we are not able to distinguish the best model among these curves. However, future data from optical, X-ray, and thermal and kinetic Sunyaev-Zel'dovich observations are expected to put significantly tighter constraints on the level of baryonic feedback (Battaglia et al. 2012; Hill et al. 2016; Amodeo et al. 2020), and these constraints can then be compared with the WL data.

## 4 CONCLUSIONS

The uncertainty in modelling baryons is already limiting the cosmological analysis with current-generation WL surveys (Abbott et al. 2018). If left unaccounted for, the effects of baryons will significantly bias our constraints on dark energy, dark matter, and neutrino mass from upcoming surveys. In this work, we generate a suite of mock WL maps, the  $\kappa$ TNG, by ray tracing through the IllustrisTNG hydrodynamic simulations. We produced 10 000 pseudo-independent maps at a wide source redshift range of  $0.034 \leq z_s \leq 2.568$ , well covering the range probed by existing and upcoming WL surveys. Furthermore, we also generate the  $\kappa$ TNG-Dark maps from the corresponding DMO simulations. We release our mock convergence maps at our website (<http://columbialensing.org>). By comparing the pair of maps with and without baryonic physics, one can isolate the baryonic effects on the WL statistics.

We find that baryonic processes suppress the WL angular power spectrum by up to 20 per cent. Towards low redshift, the level of suppression is larger, potentially due to stronger stellar and AGN feedback; in addition, the onset of the suppression occurs at larger scales, as the same physical object extends over a larger angular scale.



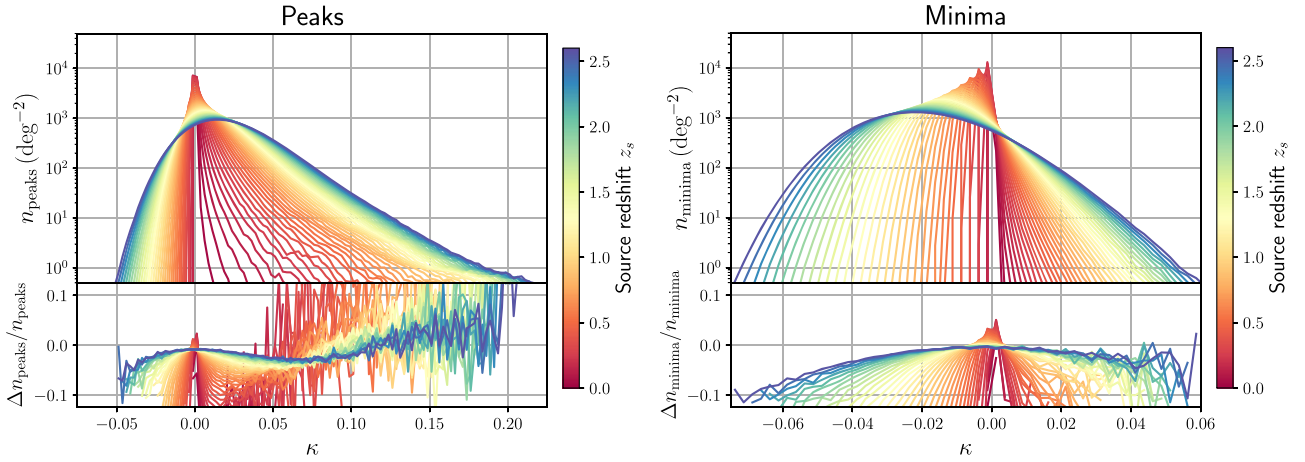


**Figure 6.** Left-hand panel: Peak counts from our  $\kappa$ TNG maps (upper panel) and the fractional differences between the  $\kappa$ TNG and  $\kappa$ TNG-Dark maps (lower panel) for all 40 source redshifts (red to blue: low to high redshifts), where  $\Delta n/n = n^{\kappa\text{TNG}}/n^{\kappa\text{TNG-Dark}} - 1$ . Right-hand panel: the same as the left, but for minimum counts. The maps are smoothed with a 2 arcmin Gaussian filter and the measurements are means over 10 000 map realizations.

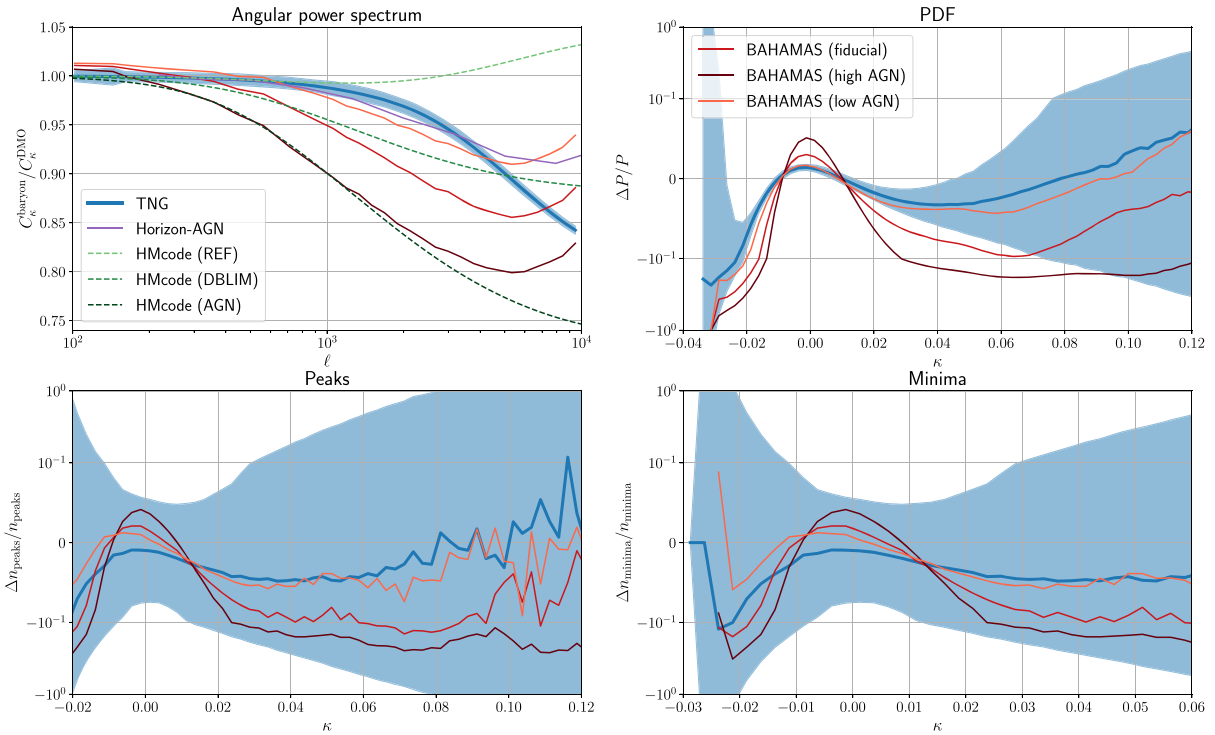


**Figure 7.** Comparison of the effects of baryonic processes on our angular power spectrum (upper left), one-point PDF (upper right), number of peaks (lower left), and number of minima (lower right) to previous works, including analytical models (dashed curves) for the power spectrum from the HMcode and hydrodynamic simulations (solid curves) BAHAMAS and Horizon-AGN. All curves are shown for  $z_s = 1$  except  $\kappa$ TNG, which source redshift is  $z_s = 1.034$  (S23). The shaded regions represent the standard deviation from 10 000  $\kappa$ TNG realizations. All maps are smoothed with a 2 arcmin Gaussian window for the PDF, peaks, and minima.

We also observe an enhancement on smaller scales due to radiative cooling. The overall suppression from  $\kappa$ TNG is moderate compared to results from other analytical models and simulations, consistent with previous works comparing their matter power spectra (Springel et al. 2018).

We also show the effects of baryons on higher order WL statistics: the PDF, peak counts, and counts of minima. These statistics contain rich non-Gaussian information beyond the power spectrum and have

the potential to place a tighter constraint on cosmological parameters with upcoming surveys. Our work is the first to show detailed redshift evolution for these statistics. In general, baryonic processes suppress both the positive and negative tails of all three statistics. The change is asymmetric on the two tails and hence is not captured by the power spectrum. In addition, we also find changes in the total number of peaks and minima. Compared to past works on baryonic effects with WL non-Gaussian statistics, mainly from the BAHAMAS

simulations, the overall trends are surprisingly similar, despite the very different subgrid models implemented in these simulations.

While contributing to a large body of semi-analytical tools and hydrodynamic simulations that have already paved the road to study the effect of baryons on WL observables, our newly developed  $\kappa$ TNG suite of mock WL maps provides a venue to extend the studies to those requiring mass maps, such as non-Gaussian WL statistics and machine learning with convolutional neural networks (Schmelzle et al. 2017; Gupta et al. 2018; Fluri et al. 2019; Merten et al. 2019; Ribli, Pataki & Csabai 2019a; Ribli et al. 2019b). Our maps will also be useful for testing pioneering works on analytical models for higher order statistics (Fan, Shan & Liu 2010; Thiele et al. 2020), which, in the future, could be extended to incorporate baryonic effects. With the  $\kappa$ TNG and  $\kappa$ TNG-Dark map pairs, one can also learn the DMO-to-hydrodynamic mapping using the generative adversarial network or variational auto-encoder (see e.g. Tröster et al. 2019) and augment existing DMO simulations. It is also possible to explore physically motivated mapping methods, similar to the gradient-descent method adopted by Dai et al. (2018) for the three-dimensional density field.

## ACKNOWLEDGEMENTS

We are grateful to Shy Genel for his help with the IllustrisTNG simulations. We thank Ian McCarthy for sharing the BAHAMAS convergence maps. We thank Will Coulton, François Lanusse, David Spergel, and Masahiro Takada for useful discussions. We thank Ryuichi Takahashi for useful comments on the earlier version of the manuscript. KO is supported by JSPS Overseas Research Fellowships. This work is in part supported by an NSF Astronomy and Astrophysics Postdoctoral Fellowship (to JL) under award AST-1602663, and by NASA through ATP grant 80NSSC18K1093 (to ZH). This work used the Extreme Science and Engineering Discovery Environment (XSEDE), which is supported by NSF Grant No. ACI-1053575.

## DATA AVAILABILITY

The data underlying this article will be partially available at Columbia Lensing (<http://columbialensing.org>), with 100 realizations for three source redshifts ( $z_s = 0.5, 1.0$ , and  $1.5$ ). The remaining data will be shared on reasonable request to the corresponding author. The simulation data of IllustrisTNG are available at <https://www.tng-project.org/>.

## REFERENCES

Abbott T. et al., 2018, *Phys. Rev. D*, 98, 43526  
 Aihara H. et al., 2018, *PASJ*, 70, S4  
 Amendola L. et al., 2018, *Living Rev. Relativ.*, 21, 2  
 Amodeo S. et al., 2020, preprint (arXiv:2009.05558)  
 Aricò G., Angulo R. E., Hernández-Monteagudo C., Contreras S., Zennaro M., 2020a, preprint (arXiv:2009.14225)  
 Aricò G., Angulo R. E., Hernández-Monteagudo C., Contreras S., Zennaro M., Pellejero-Ibañez M., Rosas-Guevara Y., 2020b, *MNRAS*, 495, 4800  
 Bartelmann M., Schneider P., 2001, *Phys. Rep.*, 340, 291  
 Battaglia N., Bond J. R., Pfrommer C., Sievers J. L., 2012, *ApJ*, 758, 74  
 Blandford R., Narayan R., 1986, *ApJ*, 310, 568  
 Chisari N. E. et al., 2019, *Open J. Astrophys.*, 2, 4  
 Cooray A., Sheth R., 2002, *Phys. Rep.*, 372, 1  
 Coulton W. R., Liu J., McCarthy I. G., Osato K., 2020, *MNRAS*, 495, 2531  
 Dai B., Feng Y., Seljak U., 2018, *J. Cosmol. Astropart. Phys.*, 2018, 009  
 Dark Energy Survey Collaboration, 2016, *MNRAS*, 460, 1270

de Jong J. T. A. et al., 2015, *A&A*, 582, A62  
 Dietrich J. P., Hartlap J., 2010, *MNRAS*, 402, 1049  
 Dubois Y. et al., 2014, *MNRAS*, 444, 1453  
 Eifler T., Krause E., Dodelson S., Zentner A. R., Hearin A. P., Gnedin N. Y., 2015, *MNRAS*, 454, 2451  
 Fan Z., Shan H., Liu J., 2010, *ApJ*, 719, 1408  
 Fluri J., Kacprzak T., Lucchi A., Refregier A., Amara A., Hofmann T., Schneider A., 2019, *Phys. Rev. D*, 100, 063514  
 Foreman S., Coulton W., Villaescusa-Navarro F., Barreira A., 2020, *MNRAS*, 498, 2887  
 Gouin C. et al., 2019, *A&A*, 626, A72  
 Gupta A., Matilla J. M. Z., Hsu D., Haiman Z., 2018, *Phys. Rev. D*, 97, 103515  
 Hannestad S., Upadhye A., Wong Y. Y. Y., 2020, *JCAP*, 11, 062H  
 Harnois-Déraps J., van Waerbeke L., Viola M., Heymans C., 2015, *MNRAS*, 450, 1212  
 Harnois-Déraps J. et al., 2018, *MNRAS*, 481, 1337  
 Harnois-Déraps J., Giblin B., Joachimi B., 2019, *A&A*, 631, A160  
 Heymans C. et al., 2021, *A&A*, 646A, 140H  
 Hikage C. et al., 2019, *PASJ*, 71, 43  
 Hilbert S., Hartlap J., White S. D. M., Schneider P., 2009, *A&A*, 499, 31  
 Hildebrandt H. et al., 2017, *MNRAS*, 465, 1454  
 Hill J. C., Ferraro S., Battaglia N., Liu J., Spergel D. N., 2016, *Phys. Rev. Lett.*, 117, 051301  
 Hoekstra H., Jain B., 2008, *Annu. Rev. Nucl. Part. Sci.*, 58, 99  
 Huang H.-J., Eifler T., Mandelbaum R., Dodelson S., 2019, *MNRAS*, 488, 1652  
 Huang H.-J. et al., 2021, *MNRAS*, 467H  
 Jain B., Seljak U., White S., 2000, *ApJ*, 530, 547  
 Kacprzak T. et al., 2016, *MNRAS*, 463, 3653  
 Kilbinger M., 2015, *Rep. Prog. Phys.*, 78, 086901  
 Kratochvil J. M., Haiman Z., May M., 2010, *Phys. Rev. D*, 81, 043519  
 Laureijs R. et al., 2011, preprint (arXiv:1110.3193)  
 Lesgourgues J., Pastor S., 2006, *Phys. Rep.*, 429, 307  
 Liu J., Petri A., Haiman Z., Hui L., Kratochvil J. M., May M., 2015a, *Phys. Rev. D*, 91, 063507  
 Liu X. et al., 2015b, *MNRAS*, 450, 2888  
 Liu J., Haiman Z., 2016, *Phys. Rev. D*, 94, 043533  
 Liu J., Hill J. C., Sherwin B. D., Petri A., Böhm V., Haiman Z., 2016, *Phys. Rev. D*, 94, 103501  
 Liu J., Bird S., Matilla J. M. Z., Hill J. C., Haiman Z., Madhavacheril M. S., Spergel D. N., Petri A., 2018, *J. Cosmol. Astropart. Phys.*, 2018, 49  
 Liu J., Madhavacheril M. S., 2019, *Phys. Rev. D*, 99, 083508  
 LSST Science Collaboration, 2009, preprint (arXiv:0912.0201)  
 McCarthy I. G., Schaye J., Bird S., Le Brun A. M. C., 2017, *MNRAS*, 465, 2936  
 McCarthy I. G., Bird S., Schaye J., Harnois-Déraps J., Font A. S., van Waerbeke L., 2018, *MNRAS*, 476, 2999  
 Mandelbaum R., 2018, *ARA&A*, 56, 393  
 Mandelbaum R. et al., 2018, *PASJ*, 70, S25  
 Marinacci F. et al., 2018, *MNRAS*, 480, 5113  
 Martinet N. et al., 2018, *MNRAS*, 474, 712  
 Maturi M., Angrick C., Pace F., Bartelmann M., 2010, *A&A*, 519, A23  
 Mead A. J., Peacock J. A., Heymans C., Joudaki S., Heavens A. F., 2015, *MNRAS*, 454, 1958  
 Merten J., Giocoli C., Baldi M., Meneghetti M., Peel A., Lalande F., Starck J.-L., Pettorino V., 2019, *MNRAS*, 487, 104  
 Mohammed I., Martizzi D., Teyssier R., Amara A., 2014, preprint (arXiv:1410.6826)  
 Naiman J. P. et al., 2018, *MNRAS*, 477, 1206  
 Nelson D. et al., 2018, *MNRAS*, 475, 624  
 Nelson D. et al., 2019, *Comput. Astrophys. Cosmol.*, 6, 2  
 Osato K., Shirasaki M., Yoshida N., 2015, *ApJ*, 806, 186  
 Patton K., Blazek J., Honscheid K., Huff E., Melchior P., Ross A. J., Suchyta E., 2017, *MNRAS*, 472, 439  
 Petri A., Haiman Z., May M., 2016, *Phys. Rev. D*, 93, 063524  
 Pillepich A. et al., 2018, *MNRAS*, 475, 648  
 Planck Collaboration XIII, 2016, *A&A*, 594, A13

- Ribli D., Pataki B. Á., Csabai I., 2019a, *Nat. Astron.*, 3, 93  
 Ribli D., Pataki B. Á., Zorrilla Matilla J. M., Hsu D., Haiman Z., Csabai I., 2019b, *MNRAS*, 490, 1843  
 Rudd D. H., Zentner A. R., Kravtsov A. V., 2008, *ApJ*, 672, 19  
 Schaye J. et al., 2010, *MNRAS*, 402, 1536  
 Schaye J. et al., 2015, *MNRAS*, 446, 521  
 Schmelzle J., Lucchi A., Kacprzak T., Amara A., Sgier R., Réfrégier A., Hofmann T., 2017, preprint ([arXiv:1707.05167](https://arxiv.org/abs/1707.05167))  
 Schneider A., Teyssier R., 2015, *J. Cosmol. Astropart. Phys.*, 2015, 049  
 Schneider A., Teyssier R., Stadel J., Chisari N. E., Le Brun A. M. C., Amara A., Refregier A., 2019, *J. Cosmol. Astropart. Phys.*, 2019, 020  
 Schneider A., Stoira N., Refregier A., Weiss A. J., Knabenhans M., Stadel J., Teyssier R., 2020, *J. Cosmol. Astropart. Phys.*, 2020,  
 Seitz S., Schneider P., Ehlers J., 1994, *Class. Quantum Gravity*, 11, 2345  
 Semboloni E., Hoekstra H., Schaye J., van Daalen M. P., McCarthy I. G., 2011, *MNRAS*, 417, 2020  
 Semboloni E., Hoekstra H., Schaye J., 2013, *MNRAS*, 434, 148  
 Shan H. et al., 2018, *MNRAS*, 474, 1116  
 Smith R. E. et al., 2003, *MNRAS*, 341, 1311  
 Somerville R. S., Davé R., 2015, *ARA&A*, 53, 51  
 Springel V., 2010, *MNRAS*, 401, 791  
 Springel V. et al., 2018, *MNRAS*, 475, 676  
 Takahashi R., Oguri M., Sato M., Hamana T., 2011, *ApJ*, 742, 15  
 Takahashi R., Sato M., Nishimichi T., Taruya A., Oguri M., 2012, *ApJ*, 761, 152  
 Takahashi R., Hamana T., Shirasaki M., Namikawa T., Nishimichi T., Osato K., Shiroyama K., 2017, *ApJ*, 850, 24  
 Thiele L., Hill J. C., Smith K. M., 2020, *Phys. Rev. D*, 102, 123545  
 Tröster T., Ferguson C., Harnois-Déraps J., McCarthy I. G., 2019, *MNRAS*, 487, L24  
 Vale C., White M., 2003, *ApJ*, 592, 699  
 van Daalen M. P., Schaye J., Booth C. M., Dalla Vecchia C., 2011, *MNRAS*, 415, 3649  
 van Daalen M. P., McCarthy I. G., Schaye J., 2020, *MNRAS*, 491, 2424  
 Vogelsberger M. et al., 2014, *Nature*, 509, 177  
 Vogelsberger M., Marinacci F., Torrey P., Puchwein E., 2020, *Nat. Rev. Phys.*, 2, 42  
 Wang S., Haiman Z., May M., 2009, *ApJ*, 691, 547  
 Wei C. et al., 2018, *ApJ*, 853, 25  
 Weiss A. J., Schneider A., Sgier R., Kacprzak T., Amara A., Refregier A., 2019, *J. Cosmol. Astropart. Phys.*, 2019, 011  
 Yang X., Kratochvil J. M., Wang S., Lim E. A., Haiman Z., May M., 2011, *Phys. Rev. D*, 84, 043529  
 Yang X., Kratochvil J. M., Huppenberger K., Haiman Z., May M., 2013, *Phys. Rev. D*, 87, 023511  
 Zentner A. R., Semboloni E., Dodelson S., Eifler T., Krause E., Hearin A. P., 2013, *Phys. Rev. D*, 87, 043509

## APPENDIX A: FITTING FORMULA FOR THE POWER SPECTRUM RATIO

We provide a fitting formula that allows a quick exploration of baryonic effects on the angular power spectrum:

$$C_{\kappa}^{\text{baryon}}(\ell)/C_{\kappa}^{\text{DMO}}(\ell) = R^{\text{fit}}(\ell) \equiv \frac{1 + (\ell/\ell_{s1})^{\alpha_1}}{1 + (\ell/\ell_{s2})^{\alpha_2}}, \quad (\text{A1})$$

where  $\ell_{s1}$ ,  $\ell_{s2}$ ,  $\alpha_1$ , and  $\alpha_2$  are redshift-dependent free parameters. Their values are tabulated in Table A1. In optimizing the fitting formula, we excluded measurements of  $\ell = 3771.0$ –9465.6 for the first source redshift  $z_s = 0.034$  (S1) because of strong artefacts due to resolution. In Fig. A1, we show the comparison of angular power spectrum ratio with  $\kappa$ TNG and the fitting formula for  $z_s = 0.506$  (S13), 1.034 (S23), and 1.989 (S35). The accuracy of the fitting formula is better than 0.3 per cent for most source redshifts of  $\kappa$ TNG maps, but slightly worse for low source redshifts.

**Table A1.** The parameters of the power spectrum fitting formula equation (A1).

Source plane	$z_s$	$\ell_{s1}$	$\ell_{s2}$	$\alpha_1$	$\alpha_2$
S1	0.034	582.64	441.63	1.693	1.478
S2	0.070	3773.54	2529.39	1.284	0.939
S3	0.105	2921.87	2104.38	1.459	1.224
S4	0.142	3250.72	2438.22	1.572	1.364
S5	0.179	3724.26	2855.09	1.645	1.452
S6	0.216	4201.42	3267.03	1.710	1.523
S7	0.255	4664.31	3663.60	1.762	1.578
S8	0.294	5119.63	4051.22	1.808	1.624
S9	0.335	5600.60	4456.01	1.846	1.657
S10	0.376	6069.34	4852.78	1.877	1.684
S11	0.418	6559.00	5264.39	1.902	1.703
S12	0.462	7099.52	5712.55	1.923	1.714
S13	0.506	7698.22	6203.65	1.940	1.720
S14	0.552	8318.01	6711.92	1.956	1.722
S15	0.599	8945.57	7227.90	1.970	1.722
S16	0.648	9577.85	7749.58	1.983	1.721
S17	0.698	10 217.52	8279.71	1.994	1.718
S18	0.749	10 859.85	8815.16	2.005	1.714
S19	0.803	11 488.44	9343.56	2.014	1.710
S20	0.858	12 086.34	9851.46	2.021	1.706
S21	0.914	12 635.92	10 323.82	2.026	1.702
S22	0.973	13 128.47	10 751.96	2.028	1.700
S23	1.034	13 551.94	11 124.61	2.027	1.698
S24	1.097	13 890.45	11 427.82	2.023	1.698
S25	1.163	14 127.45	11 647.41	2.016	1.700
S26	1.231	14 257.10	11 778.76	2.006	1.704
S27	1.302	14 279.51	11 822.83	1.993	1.709
S28	1.375	14 210.38	11 794.04	1.978	1.715
S29	1.452	14 075.06	11 714.29	1.964	1.721
S30	1.532	13 900.02	11 605.36	1.950	1.727
S31	1.615	13 698.63	11 477.60	1.937	1.734
S32	1.703	13 478.39	11 336.30	1.926	1.740
S33	1.794	13 238.19	11 179.64	1.915	1.746
S34	1.889	12 987.06	11 014.19	1.906	1.752
S35	1.989	12 729.72	10 843.22	1.898	1.758
S36	2.094	12 465.76	10 665.78	1.890	1.764
S37	2.203	12 195.18	10 481.52	1.883	1.769
S38	2.319	11 919.66	10 291.42	1.877	1.774
S39	2.440	11 641.09	10 096.77	1.871	1.779
S40	2.568	11 362.87	9900.14	1.866	1.784

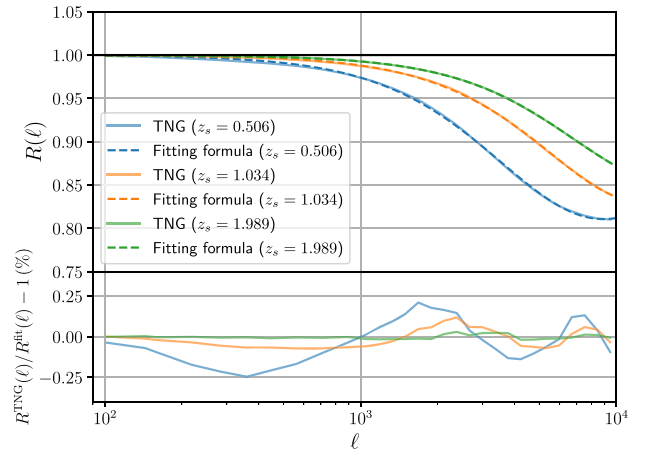


**Figure A1.** Upper panel: Comparison of angular power spectrum ratios measured from  $\kappa$ TNG and the fitting formula for three source redshifts  $z_s = 0.506$ , 1.034, and 1.989. Lower panel: Fractional differences between  $\kappa$ TNG and the fitting formula.